Chemical Science

Accepted Manuscript

This article can be cited before page numbers have been issued, to do this please use: X. Liu, J. Tang, D. Bin, Q. Huang, C. Li, L. Su, W. Qin, Y. Ge, X. Chen, H. Lu, B. Yang and Y. Wang, *Chem. Sci.*, 2026, DOI: 10.1039/D5SC07530K.

ROYAL SOCIETY OF CHEMISTRY

rsc.li/chemical-science

View Article Online
DOI: 10.1039/D5SC07530K

ARTICLE

Membrane-Free Two-Step Water Electrolysis Enable by A Stable Organic Redox Mediator

Received 00th January 20xx,
Accepted 00th January 20xx

DOI: 10.1039/x0xx00000x

Xiao Liu[a], Jinlan Tang[a], Duan Bin[a*], Qiang Huang[a], Congcong Li[a], Linyan Su[a], Wei Qin[a], Yu Ge[a], Xingru Chen[a], Hongbin Lu[a], BeiBei Yang[a*] and Yonggang Wang[b*]

Electrochemical decoupled water splitting utilizes a solid-state redox mediator (SSRM) to reversibly store proton-electron pairs, thereby separating hydrogen and oxygen evolution without the use of membrane and promoting the conversion of sustainable energy sources into hydrogen. However, the widespread appalication of this apporach is currently limited by issue such as instabilty and discontinuty of SSRM. Herein, a novel and membrane-free system is designed for decoupled hydrogen production in acidic medium, based on the highly reversible SSRM of sustainable quinone-based organic polymer (P-ACD). Due to intramolecular hydrogen bonds, the P-ACD-electrode with low loading (1-2 mg cm^{-2}) exhibits high discharged specific capability (215.32 mAh g^{-1} at 0.2 A g^{-1}), ultrafast chargeability (86.90 mAh g^{-1} at 100 A g^{-1}, just 3.12 s), and exceptional cyclability over 30,000 cycles. More importantly, Two-step water electrolysis under high loading achieves a remarkable coulombic efficiency of nearly 100% even after 600 consecutive cycles, concurrently exhibiting favorable cycle stability surpassing 184 h for hydrogen production. Consequently, this system provides a new avernue for achieving operational flexibility and membrane -free hydrogen production.

Introduction

Green hydrogen can greatly contribute to carbon neutrality, as it possesses many prominent benefits, such as high energy density and zero pollution emission.[1–4] Water electrolysis is capable of producing eco-friendly hydrogen with an impressive energy density of 143 MJ kg^{-1}, and it is estimated that by 2050, approximately 70% of hydrogen will be produced via this process, powered by renewable energy sources.[5–7] Among the various water electrolysis technologies, proton exchange membrane (PEM) electrolyzer holds its notable advantages, including higher hydrogen purity and current density, superior efficiency and compact cell design.[8,9] However, this electrolysis faces challenges such as high costs arising from the PEM, and poor durability stemming from the sluggish anodic oxygen revolution reaction (OER) and the degradation of catalysts in acidic media,[10] which widely limits their practical applications. Noticably, a persistent challenge in conventional water-splitting systems is gas crossover at low current densities, which can lead to the formation of an explosive H_2/O_2 mixture.[11] Thus, it is imperative to develop membrane-free acidic water electrolysis, wherein the release of H_2 and O_2 occurs independently in both time and space. With these considerations in mind, Cronin et al.[11] pioneered the utilization of polyoxometalate $H_3PMo_{12}O_{40}$ as a solid-state redox mediator (SSRM), which afforded some new insight into achieving the temporal and spatial decoupling of the H_2 and O_2 in PEM water electrolysis. In addition, some inorganic redox mediators, e. g., $Ni(OH)_2$ (nickel hydroxide),[12] $H_4[SiW_{12}O_{40}]$ (silicotungstic acid),[13] $Na_4[Fe(CN)_6]$ (sodium ferrocyanide)[14] have been explored for decoupling water electrolysis. It is worth noting that organic materials, endowed with high design flexibility, environmental sustainability, and cost efficiency, have rarely gained widespread utilization as SSRM in the realm of decoupling water electrolysis.[15–17]

Encouragingly, quinone-based organic compounds are remarkable for their high theoretical capacity, advantageous redox potentials, and swift reaction kinetics, which can be attributed to the enolization reaction occurring in the carbonyl redox chemistry between C=O and $C\text{-}O^-$ groups.[18] So far, Ma et al.[19] have presented pyrene-4, 5, 9, 10-tetraone (PTO) as a SSRM to separate the HER and OER in an acidic environment, achieving an electrolysis time of approximately 70.7 h for cycle stability. Meanwhile, Huang et al.[20] have designed a pseudocapacitive electrode based on dibenzo[b, i]phenazine-5, 7, 12, 14-tetrone (DPT) that is capable of decoupling acidic water electrolysis, with the electrolysis time for cycle stability reaching over 100 h. Although the above organic electrodes in SSRM is systems to decouple water electrolysis have been reported, most of them inclined to suffer from solubility and demonstrated limited cycling life (<10000 cycles) and decoupled time (<150 h). It is doubted that the long-term stability in SSRM is vital for continuous water electrolysis, which motivates the development of sustabinable organic electrode to restrain its aqueous solubility. Structurally, organic carbonyl compounds tend to dissolve in electrolytes mainly because of their inherent structural characteristics, like electron-rich aromatic units, which closely align with the polarity of electrolytes, fostering strong interactions and subsequent dissolution of the

[a]*Department of Polymer Materials and Science, College of Chemistry and Chemical Engineering, Nantong University, Nantong, 226019, China.*
E-mail: dbin17@fudan.edu.cn; yangbeibei@ntu.edu.cn
[b]*Department of Chemistry and Shanghai Key Laboratory of Molecular Catalysis and Innovative Materials, Institute of New Energy, iChEM (Collaborative Innovation Center of Chemistry for Energy Materials), Fudan University, Shanghai 200433, China.*
E-mail: ygwang@fudan.edu.cn

View Article Online DOI: 10.1039/D5SC07530K

material, thereby impairing cycling stability.[21,22] Currently, the formation of stable intramolecular hydrogen bonds (HBs) utilizing carbonyl groups represents a straightforward and effective strategy, achieved through molecular engineering design, for tackling problems such as unsatisfactory stability in carbonyl-containing organic compounds.[23] For these regards, it is highly desired to develop efficient carbonyl compounds for use in the continuous membrane-free acid water electrolysis.

Herein, an intramolecular hydrogen bonding (HB) strategy is designed, where the carbonyl groups and secondary amine groups act as multi-active centers, triggering the formation of intramolecular HBs. The intramolecular HBs in P-ACD polymer with low loading not only inhibit dissolution to enhance stability (over 30,000 cycles at 4 A g^{-1}) but also strengthen the π-conjugation effect to accelerate charge transfer, thereby improving rate capability (86.90 mAh g^{-1} at 100 A g^{-1}). In addition, the P-ACD electrode with low loading delivers a high discharge specific capacity of 215.32 mAh g^{-1}. Theoretical calculation results suggest that P-ACD experiences a sequential one-electron redox process during the reversible H^+ storage process. Then, P-ACD functions as a SSRM, effectively separating the HER and OER during acid water electrolysis. In this design, H_2 generation involves the cathodic reduction of H^+ and the anodic oxidation of P-ACD-2H (P-ACD-2H→P-ACD), whereas O_2 production depends on the cathodic reduction of P-ACD (P-ACD→P-ACD-2H) and the anodic oxidation of H_2O. Interestingly, this decoupled acidic water electrolysis system can be combined with a commercial photovoltaic power generation system, facilitating the direct conversion from solar energy and water into hydrogen.

Result and discussion

The P-ACD was synthesized using a straightforward process with a molar ratio of 5:1 between two organic monomers of 1,4-benzoquinone (monomer BQ) and 1,5-diaminonaphthalene (monomer 1,5-NAD), leading to the formation of the extended π-conjugated polymeric skeleton with a carbonyl oxygen-containing unit located in the main active area (**Fig. S1**). This molar ratio, far from merely offsetting reaction losses, proactively optimizes the efficiency of reaction synthesis. Using ethanol as the solvent proves advantageous as it can weaken the intensity of electrostatic attraction and diminish the competition of solvent molecules for N-H and C=O groups, thereby maintaining the specific intramolecular hydrogen-bonding interactions. In the Fourier-transform infrared (FTIR) spectra, the peaks at 3232 and 1573 cm^{-1}, corresponding to the stretching vibration of N-H···O bonds and C=C bonds, respectively (**Fig. 1a**). The peaks of C=O and N-H in P-ACD exhibit an obvious red shift from 1648 to 1629 cm^{-1} and from 3413 to 3361 cm^{-1}, respectively, in contrast to that observed in BQ and 1,5-NAD, assigned to the formation of the intramolecular HB (C=O···H-N).[24] In parallel, the emergence of a strong peak in the Raman spectra, corresponding to the C=O group, served as additional evidence for the formation of the quinone structure. As observed in **Fig. 1b**, the X-ray diffraction (XRD) analysis indicates that the P-ACD displayed broader characteristic peaks than the raw materials BQ and 1,5-NAD after the polymerization reaction. Moreover, thermogravimetric (TG) analysis, as depicted in **Fig. 1c**, revealed that the weight loss of the P-ACD was negligible upon heating to 140 °C, indicating a high thermal stability. The scanning electron microscopy (SEM) images (**Fig. S2**) show that the P-ACD surface morphology was composed of irregularly shaped nanoparticles. Additionally, the gel permeation chromatography (GPC) analysis further indicates a determined molecular mass of M_n=546 g mol^{-1}, M_w=1376 g mol^{-1}, along with a polydispersity index (PDI) of 2.56, and the obtained results are given in **Fig. 1d**. In the reduced density gradient (RDG) analysis, significant green spikes (marked by blue dashed circles) in the $(\lambda_2)_\rho$ range of -0.01 to 0.02 a.u. and prominent cyan-blue spikes (highlighted by red dashed circles) in the $(\lambda_2)_\rho$ range of -0.03 to 0.02 a.u. were observed, suggesting intermolecular π-π stacking interactions between adjacent aromatic planes and intramolecular hydrogen bonding within the polymeric framework, respectively (**Fig. 1e**). As shown in **Fig. S3**, the localized orbital locator-π (LOL-π) map of the naphthalene ring in P-ACD confirms the extensive conjugation and electron delocalization. Furthermore, as seen in **Fig. 1f**, the electrostatic surface potential (ESP) mapped on the van der Waals surface of P-ACD molecule reveals red regions and blue regions, corresponding to nucleophilic attack sites and electrophilic reaction centers, respectively. Specifically, the C=O group was the focus of the negative ESP, indicating a strong electrophilic tendency within this group. Then, a smaller gap (2.04 eV) between the energy levels of the lowest unoccupied molecular orbital (LUMO) and the highest occupied molecular orbital (HOMO), in comparison to BQ (3.93 eV) and 1,5-NAD (4.15 eV), serves as a clear indication of enhanced overall molecular conjugation and increased electron delocalization. Moreover, this also indicates its capacity for rapid charge transfer, as evidenced by its high electronic conductivity and superior redox kinetics (**Fig. 1g**).

View Article Online DOI: 10.1039/D5SC07530K

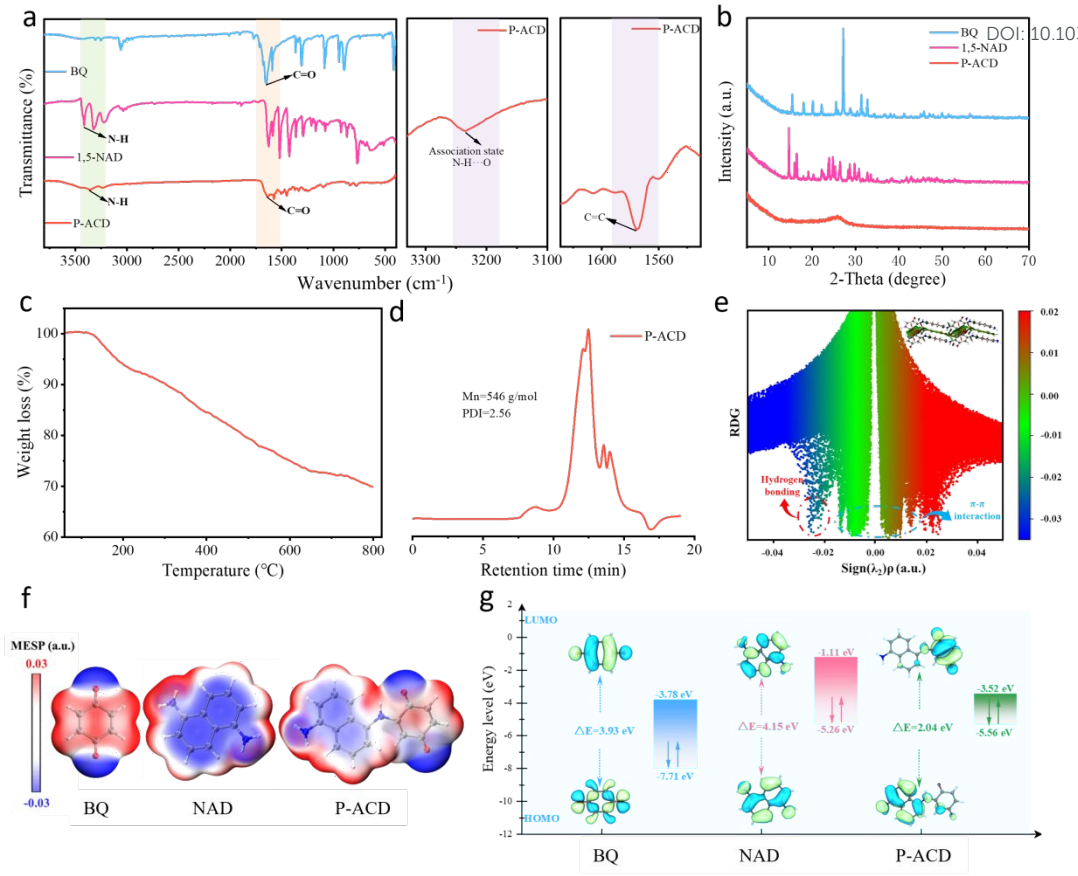

Fig 1. Synthesis and characterization of P-ACD. (a) FTIR spectra of BQ, 1,5-NAD, and P-ACD molecules. (b) XRD pattern of the BQ, 1,5-NAD, and P-ACD molecules. (c) TG of the P-ACD polymer under N_2. (d) GPC of the P-ACD polymer. (e) Plots of RDG versus sign $(\lambda_2)_\rho$ and the corresponding gradient iso-surface of the P-ACD polymer. (f) Calculated ESP distribution of the BQ, 1,5-NAD, and P-ACD molecules. (g) Calculation of the relative HOMO/LUMO energies and optimized structures of the molecules used in the DFT method calculation.

The proton-storage electrochemical performance of a designed P-ACD (SSRM) was evaluated in detail. The electrochemical activity of P-ACD electrode was first evaluated in a typical three-electrode system using 1 M H_2SO_4 as electrolyte. The cyclic voltammograms (CV) of the redox mediator P-ACD were expected to occur between the linear sweep voltammetry (LSV) curves of the HER and OER potentials based on Pt-coated Ti-mesh electrode and RuO_2/IrO_2-coated Ti-mesh electrode, confirming the fundamental principle of decoupling water electrolysis and the feasibility of P-ACD, as depicted in **Fig. 2a**. It was also noted that, the P-ACD typically underwent two successive one-electron reactions (anodic: 0.13, 0.38 V/ cathodic: 0.02, 0.21 V) that assocaited with the reversible formation of P-ACD-AH and P-ACD-2H. Furthermore, CV curves of P-ACD at different scan rate (0.2-5 mV s^{-1}) were peformed in **Fig. S4**, in which two pairs of redox peaks displayed minimal potential shifts with increasing scan rate. It was found that the relationship between the peak current *i* and scan rate *v* could be expressed by the equation $i=av^b$,[25] and the *b* values for the two pairs of redox peaks of P-ACD (denoted as a_1/c_1 and a_2/c_2) were calculated as 0.96/0.96 and 0.93/0.93, respectively (**Fig. 2b**). Strikingly, **Fig. 2c** and **Fig. S5** display that the capacitive contribution to the total capacity increased from 76.65% at 0.2 mV s^{-1} to 85.05% at 5 mV s^{-1}, corroborating the pseucapacitive-dominated charge storage behavior of the P-ACD electrode, which was underpinned by fast ionic uptake/removal kinetics.[26,27] As observed from the **Fig. S6a-b**, the exceptional ionic diffusion capability of P-ACD electrode was additionally validated through the electrochemical impedance spectroscopy (EIS) tests.[28] Furthermore, electrochemical impedance spectroscopy was utilized to analyze the kinetic behavior across distinct voltage stages of the discharge curve (**Fig. S6c-d**). Notably, the calculated diffusion coefficient in Point 1 (2.22×10^{-9} cm^2 s^{-1}) is significantly higher than that in Point 2 (4.30×10^{-10} cm^2 s^{-1}), suggesting different insertion ions during the two different discharge platforms. **Fig. 2d** demonstrates the galvanostatic charge/discharge (GCD) curves under different current densities of the P-ACD in an H^+ ion electrolyte. The specific capacities of P-ACD electrode were measured to be 179.04, 177.94, 169.02, 163.18, 157.99, 153.42, 147.42, 142.51, 137.75, 132.52, 126.30, 118.81, 109.48, 98.63, and 86.90 mAh g^{-1} at current densities of 0.2, 0.5, 1, 2, 5, 10, 20, 30, 40, 50, 60, 70, 80, 90, and 100 A g^{-1}, respectively. Moreover, the rate capability of P-ACD electrode was further evaluated, and it exhibited favorable rate performance (swift proton and electron absorption/donation capabilities) (**Fig. S7**). The charging and discharging curves of GCD demonstrate a high degree of symmetry throughout all current density conditions, indicating a highly reversible energy storage process. Notably, an area-specific capacitance of 1370.44 mF cm^{-2} is achieved at a current density of

View Article Online
DOI: 10.1039/D5SC07530K

0.30 mA cm^{-2}, highlighting its superior energy storage capacity (**Fig. S8**). **Fig. S9** presents further calculations of LUMO and HOMO for the P-ACD polymer, alongside a comparative analysis with the energy levels of other organic polymers. Impressively, the energy gap observed was markedly narrower compared to that of previously polymers with comparable molecular frameworks. Typically, a diminished HOMO-LUMO energy gap (2.04 eV) correlates with enhanced conductivity, indicating that P-ACD possesses the capability for rapid charge-carrier migration and superior reaction dynamics, which is a good agreement with the results of the rate capability tests.[29,30] By contrast, the discharge capacity of P-ACD, measured at various current densities, greatly exceeded that of most proton-storage electrodes found in other reported materials, as depicted in **Fig. 2e**.[31–37] As shown in **Fig. S10**, the P-ACD electrode exhibits a capacity retention of approximately 80% at 0.5 A g^{-1} over 400 cycles. Note that, it also achieved unprecedentedly cycling stability up to 30,000 cycles at 4 A g^{-1}, with a capacity decay rate of only 0.0023% per cycle, as evidenced by **Fig. 2f**. Consistently, the results in **Fig. S11-12** indicated that the cycling stability of the P-ACD electrode was systematically demonstrated through Nyquist plots and CV profiles over multiple cycles (1st, 5th, 10th, 15th, and 20th), with its electrochemical performance remaining at the initial level even after 20 cycles. Notably, it was clearly observed that when the P-ACD electrode was immersed in 1 M H_2SO_4 and 2 M H_2SO_4 electrolytes, there was no dissolution of it, thereby attesting to its exceptional chemical stability (**Fig. S13**). As shown in **Fig. S14**, even after long-term cycling, the P-ACD polymer was impressively stable in a 1 M H_2SO_4 electrolyte without decomposition or dissolution, confirming its excellent structural stability for storing protons repeatedly. As displayed in **Fig. 2g** and **Fig. S15**, the rate performance of P-ACD electrodes with different mass loadings. When the mass loading was increased to 31.70 mg cm^{-2} and 49.30 mg cm^{-2}, the corresponding electrodes still delivered promising capacities of 183.06 mAh g^{-1} and 177.69 mAh g^{-1}, respectively. These results indicate that the DPT electrodes can maintain their high-rate performance even under very high mass loadings. Additionally, as shown in **Fig. S16**, the highly symmetric charge-discharge curves within the current density range of 6.33 to 98.67 mA cm^{-2} demonstrate excellent charge-discharge reversibility. Additionally, the P-ACD electrode, having a high mass of 49.3 mg cm^{-2}, shows a favorable lifetime. It retains 88.8% capacity after 200 cycles at a current density of 0.67 A g^{-1} (as in **Fig. S17**). Taken together, the process of decoupling water electrolysis is integrated with a prospective SSRM candidate that is characterized by exceptional redox cyclability and superior stability in acid solution.

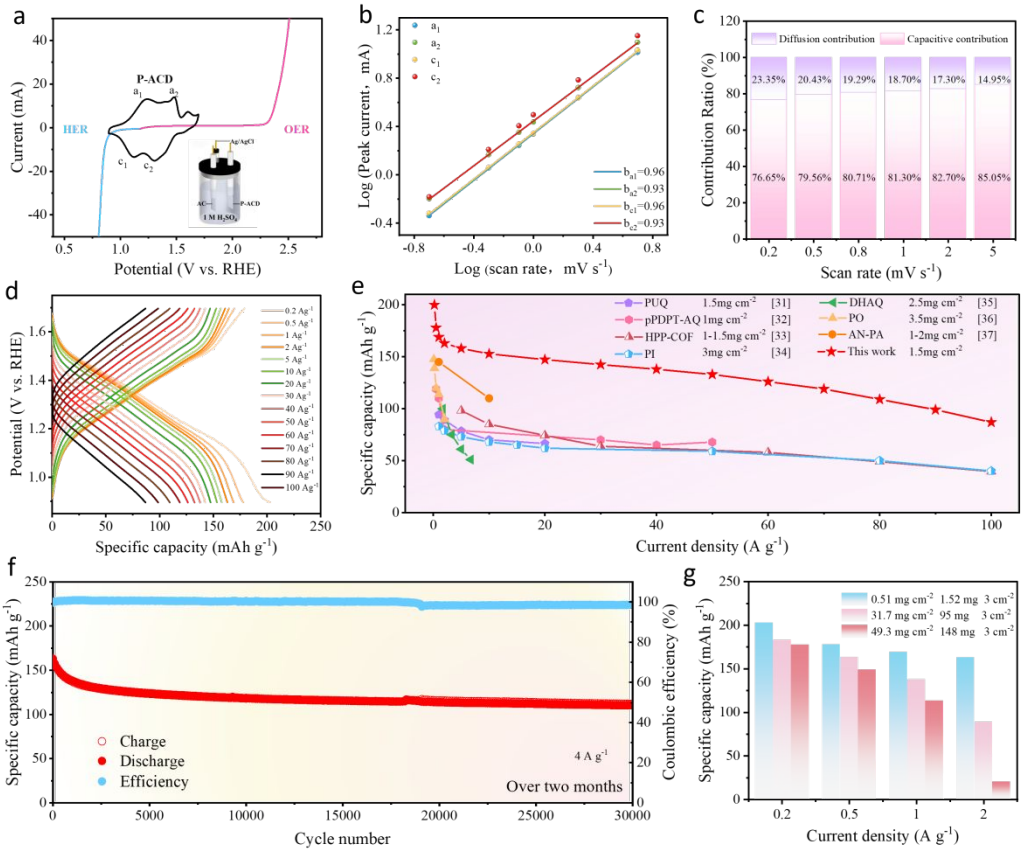

Fig 2. Electrochemical performance of the P-ACD electrode (mass loadings of 1-2 mg$_{P\text{-}ACD}$ cm^{-2}). (a) CV curve of the P-ACD film electrode (black line), the LSV data of the Pt-coated Ti-mesh electrode for the HER (blue line) and the LSV data of the commercial RuO_2/IrO_2-coated Ti-mesh electrode for the OER (pink line) at a scan rate of 5 mV s^{-1} in 1M H_2SO_4. (b) *b*-values are calculated by linearly fitting the log current vs the log scan rate. (c) Percentages of capacitive contribution at different voltage scan rates. (d) GCD curves of the P-ACD-electrode at different current

densities from 0.2 to 100 A g^{-1}. (e) Comparison of rate performance with the reported proton-storage electrodes (mass loadings of 1-3.5 mg cm^{-2}). (f) Long-term cycling stability of P-ACD electrode at a current density of 4 A g^{-1}. (g) Rate performance of P-ACD electrode with different mass-loading (0.51-49.3 $mg_{P\text{-}ACD}$ cm^{-2}).

View Article Online
DOI: 10.1039/D5SC07570K

As noted earlier, P-ACD presents excellent reversible electron and proton donor/acceptor with redox-active center thermodynamically positioned between the onset potentials of OER and HER and it can mitigate pH fluctuations in the electrolyte during HER/OER processes, thereby acting as an ideal SSRM for acid water electrolysis. To prove the viability of the decoupled hydrogen production, a hybrid energy device was assembled by a commercial Pt-coated Ti mesh electrode for HER, a commercial RuO_2/IrO_2-coated Ti mesh electrode for OER and incorporating a P-ACD film electrode to serve as a redox mediator, respectively, as schematically shown in **Fig. S18**. A general illustration of the SSRM approach based on the reversible enolization reaction of the solid-state P-ACD was given in **Fig. 3a**. The P-ACD initially underwent a reversible reduction process to attain an anionic intermediate through electron acquisition, followed by proton coordination in the 1 M H_2SO_4, ultimately forming the P-ACD-2H via a coordination reaction. In step 1, electrochemical reoxidation of the reduced SSRM (P-ACD-2H) then released the protons and electrons (P-ACD) to give H_2 at Pt-coated Ti mesh electrode, based on the reaction. In step 2, the protons and electrons were used to reduce and protonate reversibly the SSRM (P-ACD-2H) to give O_2 at RuO_2/IrO_2-coated Ti mesh electrode, based on the reaction.

To verify the practicability of decoupled amphoteric water electrolysis, chronopotentiometry measurements were conducted in 1 M H_2SO_4 to investigate the performance of this decoupled system, with applied currents density ranging from 1.67 to 100 mA cm^{-2} (**Fig. 3b-e** and **Fig. S19a-c**). The performance under varying electrolysis currents demonstrates the operational flexibility of the system, in which the electrolysis duration progressively decreases with increasing current (with the mass of P-ACD held constant, the electrolysis time for each step varies with the applied current). Furthermore, the voltages of both Step 1 and Step 2 were derived from the potential difference between the anode and cathode. The chronopotentiometry curves, showing anodic and cathodic potentials versus time, were studied during the electrolysis process at the current density of 1.67 mA cm^{-2} with a step time of 10800 s, and the results were depicted in **Fig. 3b**. Specifically, In Step 1 (H_2 generation), the average operating voltage (0.472 V) was calculated as the difference between the P-ACD oxidation anode potential (1.340 V vs. RHE) and the H^+ reduction cathode potential (0.868 V vs. RHE). For Step 2 (O_2 generation), the voltage increased to 1.092 V, determined by the H_2O oxidation anode potential (2.467 V vs. RHE) minus the HATN reduction cathode potential (1.375 V vs. RHE). Besides, the acid water electrolysis cell was investigated with an applied current of 100 mA cm^{-2} and a fixed step time of 80 s. The cell voltages during Step 1 (H_2 production) and Step 2 (O_2 production) were measured to be 1.13 V and 2.04 V, respectively, which correspond to the potential differences between the anode and cathode, as seen in **Fig. 3e**. Notably, the P-ACD electrode can operate normally under a high current density of 100 mA cm^{-2}, which is attributed to its pseudocapacitive control. This endows the electrode with rapid kinetic characteristics and high capacity, directly enhancing the overall rate of decoupled electrolysis, especially under high current density conditions.[20] As analyzed above, the fact that the electrolysis times for Step 1 and Step 2 remained identical irrespective of the current employed suggests that the electrolytic system achieved a coulombic efficiency of 100%. Remarkably, at an electrolysis current density of 1.67 mA cm^{-2}, the cell voltages for step 1 and step 2 of the electrolytic cell are 0.51 and 1.13 V, respectively, achieving an energy efficiency of 75%, was depicted in **Fig. 3f**. It is noteworthy that the photographs of Step 1 and Step 2 were presented in **Fig. S20**, and corresponding videos illustrating the independent generation of H_2 and O_2 were provided in **Videos S1** and **S2**. One can notice that P-ACD, as a mature electrode material, exhibits its high energy efficiency along with a long-lasting cycle life (184h). The stability of the electrochemical cell was evaluated to be over 600 cycles at an applied current of 1.67 mA cm^{-2}, 3.33 mA cm^{-2}, 6.67 mA cm^{-2}, 16.67 mA cm^{-2}, and 33.33 mA cm^{-2}, as shown in **Fig. 3g**. Impressively, electrolysis was carried out with varying currents and step times, i.e., 1.67 mA cm^{-2} with a step time of 4000 s for 50 cycles, 3.33 mA cm^{-2} with a step time of 2400 s for 50 cycles, 6.67 mA cm^{-2} with a step time of 1200 s for 100 cycles, 16.67 mA cm^{-2} with a step time of 800 s for 150 cycles, and 33.33 mA cm^{-2} with a step time of 400 s for 250 cycles. It was observed that the cell voltages in both Step 1 and Step 2 remained almost unchanged, indicating the exceptional stability of the system for H_2 and O_2 production. This is because the P-ACD electrode contains intramolecular HBs, which enhance intramolecular interaction forces and reduce its solubility.

To ascertain the purity of the hydrogen and oxygen generated during the individual steps, the in situ differential electrochemical mass spectrometry (DEMS) was utilized for the real-time analysis of gas evolution during the comprehensive water electrolysis process, maintained at a consistent applied current density of 33.33 mA cm^{-2} (**see Experimental Section for detail**). There was a rapid increase in the baseline signal intensity of H_2, whereas the O_2 baseline signal held steady, which concussively indicated that only the HER took place in step 1, with no observed OER occurring. Afterwards, the system was allowed to rest and was flushed with pure N_2 to eliminate any residual O_2. Likewise, as Step 2 electrolysis commenced, the O_2 baseline displayed a sharp upward trend, while the H_2 baseline signal stayed unchanged, serving as confirmation that Step 2 dedicated to OER proceeded without the simultaneous occurrence of any HER. Take together, these data implied that O_2 and H_2 evolution can be successfully decoupled from each other using P-ACD, thereby permitting direct atmospheric discharge of electrolytically generated O_2 while inherently avoiding H_2 co-production (DEME data diagram in **Fig. 3h**, the corresponding chronopotentiometry data graph in **Fig. 3i**).

View Article Online
DOI: 10.1039/D5SC07530K

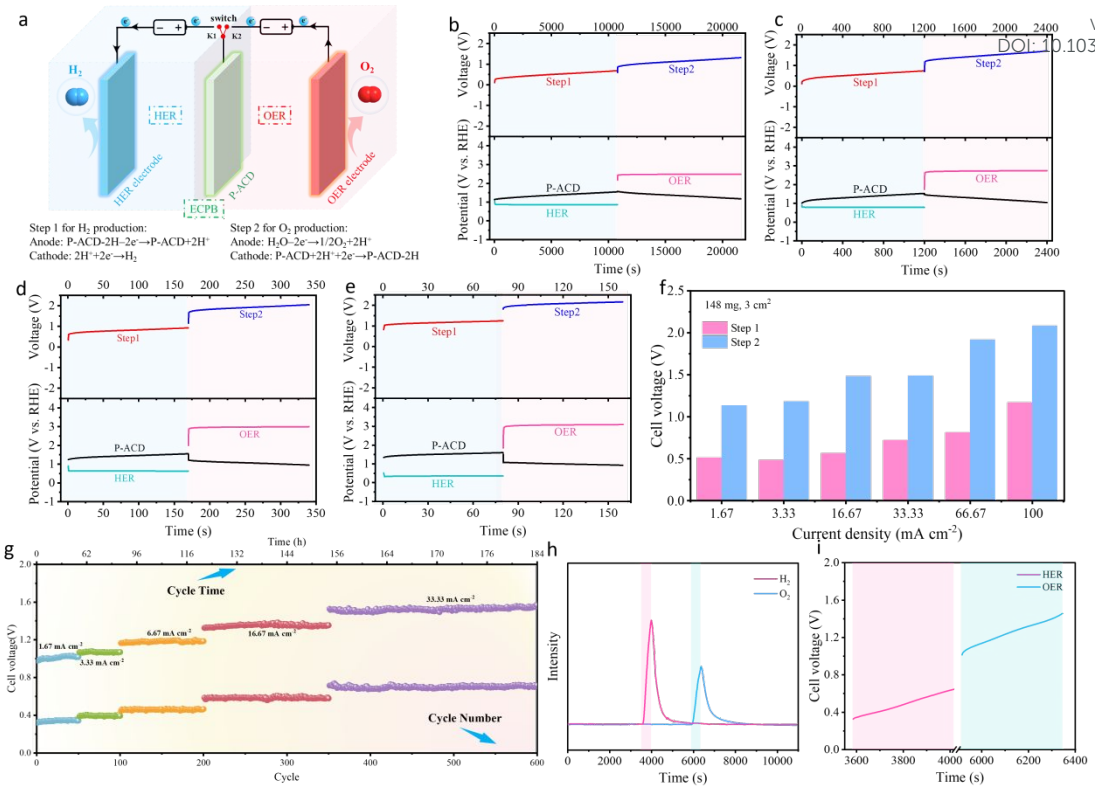

Fig 3. The decoupled water electrolysis system using P-ACD electrode as redox mediator under high loading. (a) Schematic of the decoupled water electrolysis system using P-ACD electrode as redox mediator. Chronopotentiometry curve of the decoupled cell at a current density of (b) 1.67 mA cm^{-2}, (c) 16.67 mA cm^{-2} (d) 66.67 mA cm^{-2} and (e) 100 mA cm^{-2} with a step time of 10800 s, 1200 s, 170 s and 80 s, respectively. The voltages for H_2 production (step 1) and O_2 production (step 2) are labelled by the red and blue lines, respectively. Chronopotentiometry data (potential versus time) of the OER electrode (pink line), HER electrode (green line) and P-ACD electrode (black line) are provided (mass loadings of 49.3 $mg_{P\text{-}ACD}$ cm^{-2}). (f) Cell voltages of the decoupled water electrolysis cell at each step under applied currents utilizing P-ACD electrode with a mass loading of 49.3 $mg_{P\text{-}ACD}$ cm^{-2} as a redox mediator, respectively (the cell voltage of each cycle is derived from the average value of its chronopotentiometry data). (g) The stability performance of the separate H_2/O_2 generation at 1.67 mA cm^{-2}, 3.33 mA cm^{-2}, 6.67 mA cm^{-2}, 16.67 mA cm^{-2}, and 33.33 mA cm^{-2}, is evaluated, with the cell voltage for each cycle calculated as the average value obtained from the chronopotentiometry data (mass loadings of 32.7 $mg_{P\text{-}ACD}$ cm^{-2}). (h) The production of high-purity H_2 (Step 1, indicated by the pink line) and O_2 (Step 2, indicated by the blue line) is demonstrated by the in-situ DEMS analysis and (i) the corresponding chronopotentiometry curves (voltage versus time) of the electrolytic cell at an applied current density of 33.33 mA cm^{-2}.

A P-ACD/P-ACD-2H electrode, initially unveiled as a SSRM to decouple the O_2 and H_2 evolution processes in acidic water electrolysis, has received significant attention due to its obvious advantages. In light of these results and taking into account the fact that the sequential generation of H_2 and O_2 was beneficial for the flexible utilization of renewable energy, it is reasonable to conclude that integrating the photovoltaic panel with the P-ACD-based decoupling device to form a photovoltaic water electrolysis system (**Fig. 4a, Videos S3** and **S4**). More interestingly, it can be speculated that by taking advantage of the feature of this system where H_2 and O_2 were produced at different times/locations, solar energy can be utilized for H_2 production during the day, while wind energy can be employed to drive O_2 production at night. To validate this concept, a 12 h cyclic decoupled process was designed: H_2 production during daytime and O_2 production at nighttime (**Fig. 4b-c**). Moreover, given that photovoltaic and wind power are characterized by power fluctuations, they are fundamentally incapable of maintaining a constant low current. Therefore, during the hydrogen production process, varying input current density were applied to simulate the intermittency of renewable energy sources (e.g., solar, wind, etc.). Starting from 0.33 mA cm^{-2} and stepping through 0.67, 1.67, 3.33, 8.33, 16.67, 33.33, 66.67, up to 100 mA cm^{-2}, the corresponding cell voltage remained within the range of 0–0.6 V. This result preliminarily demonstrates the operational flexibility of decoupled water electrolysis in the time domain and the continuous operational stability of the system (**Fig. S21**). Furthermore, to explore the energy consumption of the decoupled water electrolysis system using a proton buffer electrode for H_2, a drainage technique was implemented to measure the volume of H_2 produced over a defined electrolysis period, resulting in the Faraday efficiency for H_2 production (approximately 99.4%) (**Fig. 4d** and **Fig. S22**). As illustrated in **Fig. 4e**, based on the above experimental results, it can be concluded that, compared with traditional one-step water electrolysis, the energy consumption of two-step water electrolysis

View Article Online
DOI: 10.1039/D5SC07530K

was slightly lower under specific conditions. Noted that this result is derived solely from calculations based on the electrolysis voltage for water splitting and does not account for the additional energy consumption introduced by the third electrode. **Fig. S23** demonstrates that the total voltage of the two-step electrolysis under high current is slightly lower than that of the traditional proton exchange membrane electrolysis system, indicating lower energy consumption. Moreover, non-precious electrodes for OER and HER can be also utilized in the decoupled process based on the SSRM (P-ACD) mechanism (see **Fig. S24** and corresponding discussions). As contrastively depicted in the radar diagram (**Fig. 4f**), considering all factors including the time to decouple the cell at 5 mA, mass-loading, stability performance, coulombic efficiency, and applied current density, it is reasonable to expect that P-ACD outperforms the majority of other most advanced organic materials, such as PANI, PTPAn, and HATN.[38–40]

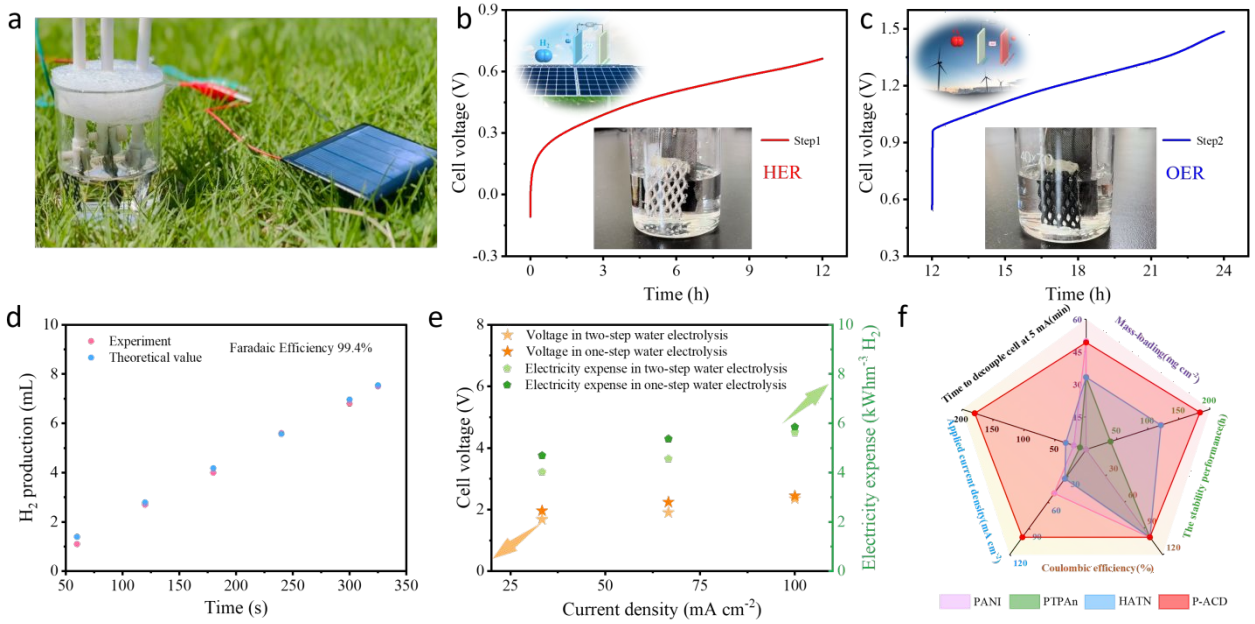

Fig 4. The decoupled water electrolysis system using P-ACD electrode as redox mediator (mass loadings of 49.3 $mg_{P\text{-}ACD}$ cm^{-2}). (a) Photo profile of the OER of the photovoltaic water electrolysis under natural sunshine. (b) hydrogen production (Step 1) during daytime (12 h at 0.33 mA cm^{-2} current density), followed by (c) oxygen production (Step 2) at nighttime (12 h at 0.33 mA cm^{-2} current density). (d) Comparison of the measured and theoretically calculated volume of H_2 during hydrogen production in HER cell at 66.67 mA cm^{-2}. Hydrogen volume is obtained using drainage method. (e) The electricity expense for H_2 production at an applied current of 33.3 mA cm^{-2}, 66.7 mA cm^{-2}, and 100 mA cm^{-2}. (f) Comparison of electrochemical performances of P-ACD and other organic solid-state redox mediators reported in the related literature.

To gain deeper insight into the mechanism of the P-ACD/P-ACD-2H reaction, a series of characterizations were conducted to monitor the structure during repeated charge/discharge processes (**Fig. 5a**). First, FTIR spectra was employed to confirm the bonding states during the charge process. **Fig. S25** shows that the adsorption peaks at around 1640 cm^{-1} for C=O groups were weakened continuously during discharging (from point c to f) and enhanced during charging (from point f to h), indicating that the active sites for H^+ coordination were C=O groups. More intuitively, an in-situ Raman spectrum also provided additional proof of the activity of C=O bonds. During charge, the characteristic peak of approximately 1680 cm^{-1} was gradually enhanced but then became progressively weaker during the discharge process, which was attributed to the change in C=O (see **Fig. 5b**). Aside from ex-situ FTIR and *in-situ* Raman spectra, ex-suit X-ray photoelectron spectroscopy (XPS) O1s (**Fig. 5c**) was utilized to analyze the P-ACD electrode at pristine, fully discharged and charged states. Notably, the characteristic peak attributed to the C=O group (533 eV) gradually disappeared at the fully discharged state and progressively increased again to a high level at the fully charged state, which was in agreement with the results observed from the in-situ experiments, disclosing the reversible redox reactions between C=O and C-O group of the P-ACD electrode during the processes of proton absorption and desorption. Furthermore, DFT calculations were conducted to investigate the redox and electron conductive mechanisms for P-ACD. It needs to point out the structures of several pertinent molecules that may participate in the reduction process of P-ACD, which was depicted in **Fig. 5d**. The simulation results depicting the most probable redox reaction pathways for the reaction between P-ACD and H^+ were shown in **Fig. 5e.** During the discharging of the P-ACD, the protonation of P-ACD occured in two steps, aligning with the observations from CV tests. Notably, only part of the P-ACD underwent further protonation as its C=O group accepts an electron via single electron transfer to form an intermediate ($C=O^-$), which then combined with H^+ to yield P-ACD-AH

or P-ACD-BH (Step 1). Subsequently, the remaining C=O group in P-ACD was protonated again, resulting in the formation of P-ACD-2H. In the discharge process (step 1) of the energy-optimized structure of P-ACD (**Fig. 5f**), the Gibbs free energy change (ΔG) value of reaction 1-1 (-0.2733 eV) was much lower than that of reaction 1-2 (0.0444 eV), suggesting that the one-electron process (P-ACD→P-ACD-AH) was more thermodynamically favorable in the step 1 due to its more negative ΔG value. Afterward, one H^+ charge carry participated in redox reaction of the step 2 in the residual carbonyl sites, resulting in the formation of P-ACD-2H. Collectively, the results obtained from theoretical calculations clearly indicate that P-ACD was subject to a redox process that consists of two consecutive one-electron transfer steps in its capacity to accommodate H^+ storage.

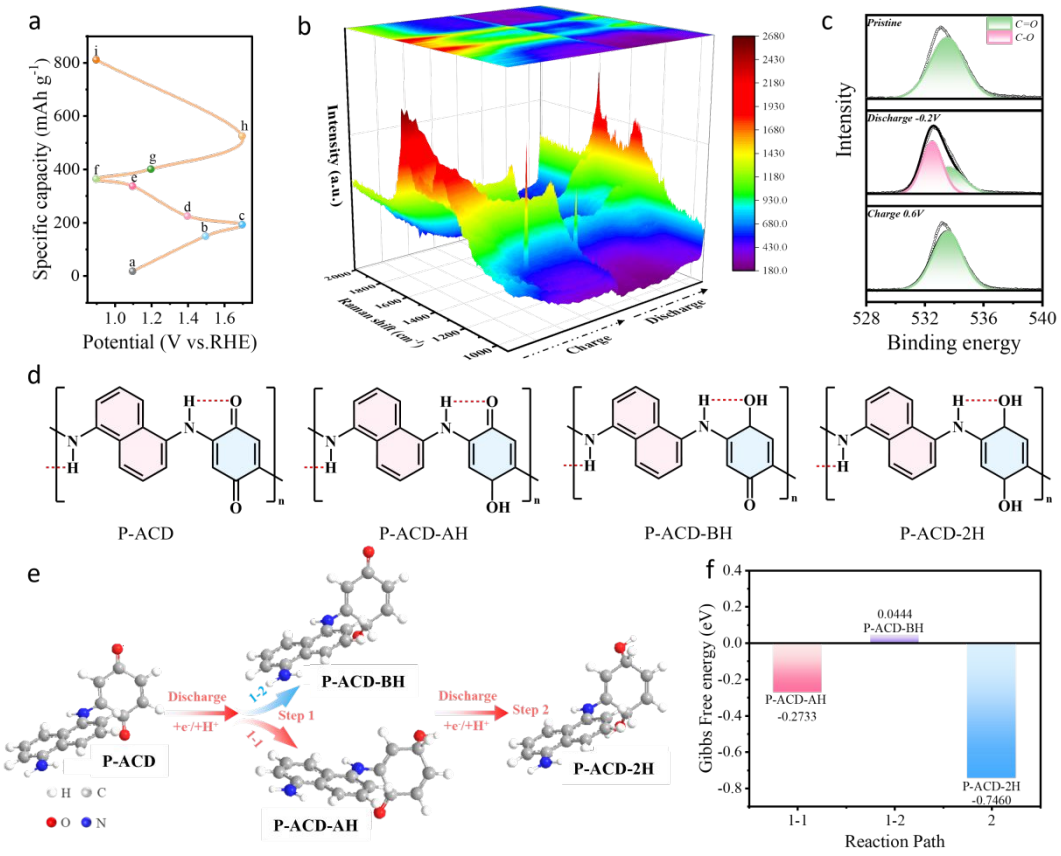

Fig 5. Structural evolution of P-ACD electrode during electrochemistry. (a) Initial charge-discharge profiles at 0.5 A g^{-1} of P-ACD. (b) In situ Raman spectrum. (c) High resolution XPS spectra of O1s at different voltage. (d) The likely configurations of several relevant molecules that are most likely to participate. (e) Calculated results concerning the redox reaction pathways of P-ACD. (f) Structural evolution of H^+-coordinated P-ACD and corresponding ΔG vaules.

Conclusions

In summary, the P-ACD/P-ACD-2H redox-coupled hydrogen production system enables membrane-free decoupled acidic water electrolysis, effectively separating hydrogen and oxygen production. Comprehensive ex-situ and in-situ characterizations reveal that the P-ACD electrode undergoes decomposition into a hydrogen donor, thereby facilitating a two-proton transfer via an enolization reaction. Owing to the presence of intramolecular hydrogen bonding, the system exhibits a high specific capacity, long-term cycling stability, and rapid chargeability. As a result, the decoupled electrolysis cell demonstrates excellent operational stability (exceeding 184 h) and ultrahigh mass loading (up to 49.33 mg cm^{-2}). By integrating this membrane-free decoupled electrolysis design with a commercial photovoltaic power generation system, spatiotemporally separated hydrogen and oxygen production has been successfully achieved. This work highlights the application of a novel organic polymer as a redox mediator to decoupled hydrogen production and offers valuable insights for the development of high-performance redox systems.

Author contributions

View Article Online
DOI: 10.1039/D5SC07570K

Xiao Liu: conducted the experiments and wrote the initial draft; Jinlan Tang, Qiang Huang, Congcong Li and Linyan Su performed the theoretical calculations; Wei Qin, Yu Ge, and Xingru Chen carried out the formal analysis; Duan Bin, Beibei Yang, and Hongbin Lu were responsible for the conceptualization, reviewing and editing the article, as well as securing the research funding; Yonggang Wang assumed the supervisory work, reviewed and edited the article.

Conflicts of interest

There are no conflicts to declare.

Data availability

Extended data supporting this article are available in the Supplementary Information.

Acknowledgements

This work was financially supported by National Natural Science Foundation of China (22309091 and 22225201).

Notes and references

1 J. Tang, C. Su and Z. Shao, Exploration, 2024, **4**, 20220112.
2 J. Liang, S. Li, X. Liu, Y. Wan, Y. Xia, H. Shi, S. Zhang, H.-L. Wang, G. Lu, G. Wu, Y. Huang and Q. Li, *Nat Catal*, 2024, **7**, 719–732.
3 J. Wei, Y. Shao, J. Xu, F. Yin, Z. Li, H. Qian, Y. Wei, L. Chang, Y. Han, J. Li and L. Gan, *Nat Commun*, 2024, **15**, 9012.
4 K. Dong and Q. Yuan, *Chem. Sci.*, 2025, **16**, 9854–9862.
5 J. Li and H. Duan, *Chem*, 2024, **10**, 3008–3039.
6 A. Odenweller, F. Ueckerdt, G. F. Nemet, M. Jensterle and G. Luderer, *Nat Energy*, 2022, **7**, 854–865.
7 M. N. Lakhan, A. Hanan, Y. Wang, H. K. Lee and H. Arandiyan, *Chem. Sci.*, 2024, **15**, 15540–15564.
8 J. Kibsgaard and I. Chorkendorff, *Nat Energy*, 2019, **4**, 430–433.
9 E. A. Toledo-Carrillo, M. García-Rodríguez, L. M. Sánchez-Moren and J. Dutta, *Sci. Adv.*, **10**, eadi3180.
10 Y. Xu, Z. Mao, J. Zhang, J. Ji, Y. Zou, M. Dong, B. Fu, M. Hu, K. Zhang, Z. Chen, S. Chen, H. Yin, P. Liu and H. Zhao, *Angew. Chem. Int. Ed.*, 2024, **63**, e202316029.
11 B. Rausch, M. D. Symes, G. Chisholm and L. Cronin, *Science*, 2014, **345**, 1326–1330.
12 X. Yan, J. Biemolt, K. Zhao, Y. Zhao, X. Cao, Y. Yang, X. Wu, G. Rothenberg and N. Yan, *Nat Commun*, 2021, **12**, 4143.
13 J. Lei, J. Yang, T. Liu, R. Yuan, D. Deng, M. Zheng, J. Chen, L. Cronin and Q. Dong, *Chem. Eur. J.*, 2019, **25**, 11432–11436.
14 W. Li, N. Jiang, B. Hu, X. Liu, F. Song, G. Han, T. J. Jordan, T. B. Hanson, T. L. Liu and Y. Sun, *Chem*, 2018, **4**, 637–649.
15 S. Wu, M. Taylor, H. Guo, S. Wang, C. Han, J. Vongsvivut, Q. Meyer, Q. Sun, J. Ho and C. Zhao, *Angew. Chem. Int. Ed.*, 2024, **63**, e202412455.
16 C. Wang, D. He, H. Wang, J. Guo, Y. Feng, L. Hu, C. Zheng, M. Zhao, X. Wang and Y. Wang, *Adv. Sci.* , 2024, **11**, 2401314.
17 H. Cui, D. Zhang, Z. Wu, J. Zhu, P. Li, C. Li, Y. Hou, R. Zhang, X. Wang, X. Jin, S. Bai and C. Zhi, *Energy Environ. Sci.*, 2024, **17**, 114–122.
18 C. Peng, F. Wang, Q. Chen, X. Yan, C. Wu, J. Zhang, W. Tang, L. Chen, Y. Wang, J. Mao, S. Dou and Z. Guo, *Adv Funct Mater.*, 2024, **34**, 2401001.
19 Y. Ma, Z. Guo, X. Dong, Y. Wang and Y. Xia, *Angew. Chem. Int. Ed.*, 2019, **131**, 4670–4674.
20 X. Huang, T. Kong, Z. Li, X. Yu, C. Liu, Z. Wang and Y. Wang, *Adv Funct Materials*, 2025, 2425176.
21 Q. Zhao, Z. Zhu and J. Chen, *Adv. Mater.*, 2017, **29**, 1607007.
22 Z. Song, W. Liu, Q. Huang, Y. Lv, L. Gan and M. Liu, *Chem. Sci.*, 2025, **16**, 16542–16551.
23 C. Ding, Y. Zhao, W. Yin, F. Kang, W. Huang and Q. Zhang, *Angew. Chem. Int. Ed.*, 2025, **64**, e202417988.
24 Z. Lin, H.-Y. Shi, L. Lin, X. Yang, W. Wu and X. Sun, *Nat Commun*, 2021, **12**, 4424.
25 Q. Sun, T. Sun, J. Du, K. Li, H. Xie, G. Huang and X. Zhang, *Adv. Mater.*, 2023, **35**, 2301088.
26 S. Xu, J. Wu, X. Wang and Q. Zhang, *Chem. Sci.*, 2023, **14**, 13601–13628.
27 X. Qiu, J. Xu, K. Zhou, X. Huang, M. Liao, Y. Cao, G. Zhou, P. Wei and Y. Wang, *Angew. Chem. Int. Ed.*, 2023, **62**, e202304036.
28 Y. Zhao, K. Feng and Y. Yu, J. Energy Chem., 2025, **102**, 524–533.
29 Z. Song, L. Miao, H. Duan, Y. Lv, L. Gan and M. Liu, *Angew. Chem. Int. Ed.*, 2024, **63**, e202401049.
30 H. Peng, J. Xiao, Z. Wu, L. Zhang, Y. Geng, W. Xin, J. Li, Z. Yan, K. Zhang and Z. Zhu, *CCS Chem*, 2023, **5**, 1789–1801.
31 M. Zhu, L. Zhao, Q. Ran, Y. Zhang, R. Peng, G. Lu, X. Jia, D. Chao and C. Wang, *Adv. Sci.*, 2022, **9**, 2103896.
32 X. Wang, J. Zhou and W. Tang, *Energy Storage Mater.*, 2021, **36**, 1–9.
33 Y. Lin, H. Cui, C. Liu, R. Li, S. Wang, G. Qu, Z. Wei, Y. Yang, Y. Wang, Z. Tang, H. Li, H. Zhang, C. Zhi and H. Lv, *Angew. Chem. Int. Ed.*, 2023, **62**, e202218745.
34 W. Han, M. Li, Y. Ma and J. Yang, *Electrochim. Acta.*, 2022, **403**, 139550.
35 J. Yu, J. Li, Z. Y. Leong, D. Li, J. Lu, Q. Wang and H. Y. Yang, *Mater. Today Energy.*, 2021, **22**, 100872.
36 Z. Tie, S. Deng, H. Cao, M. Yao, Z. Niu and J. Chen, *Angew. Chem. Int. Ed.*, 2022, **61**, e202115180.
37 K. C. S. Lakshmi, B. Vedhanarayanan, H.-Y. Cheng, X. Ji, H.-H. Shen and T.-W. Lin, *J. Colloid Interface Sci.*, 2022, **619**, 123–131.
38 J. Wang, L. Ji, X. Teng, Y. Liu, L. Guo and Z. Chen, *J. Mater. Chem. A*, 2019, **7**, 13149–13153.
39 Y. Ma, X. Dong, Y. Wang and Y. Xia, *Angew. Chem. Int. Ed.*, 2018, **57**, 2904–2908.
40 K. Wu, H. Li, S. Liang, Y. Ma and J. Yang, *Angew. Chem. Int. Ed.*, 2023, **135**, e202303563.

View Article Online
DOI: 10.1039/D5SC07530K

Data availability

Extended data supporting this article are available in the Supplementary Information.